

Grain Boundaries in Graphene on SiC(000 $\bar{1}$)

Substrate

Yann Tison,^{†,§} Jérôme Lagoute,^{*,†} Vincent Repain,[†] Cyril Chacon,[†] Yann Girard,[†]
Frédéric Joucken,[‡] Robert Sporken,[‡] Fernando Gargiulo,[¶] Oleg V. Yazyev,[¶] and
Sylvie Rousset[†]

*Laboratoire Matériaux et Phénomènes Quantiques, Université Paris Diderot-Paris 7, Sorbonne
Paris Cité, CNRS, UMR 7162,
10, rue A. Domon et L. Duquet, 75205 Paris 13, France, Research Center in Physics of Matter
and Radiation (PMR), Université de Namur, 61 Rue de Bruxelles, 5000 Namur, Belgium, and
Institute of Theoretical Physics, Ecole Polytechnique Fédérale de Lausanne (EPFL), CH-1015
Lausanne, Switzerland*

E-mail: jerome.lagoute@univ-paris-diderot.fr

KEYWORDS: graphene, grain boundaries, scanning tunneling microscopy, scanning tunneling spectroscopy

Abstract

^{*}To whom correspondence should be addressed

[†]Laboratoire Matériaux et Phénomènes Quantiques, Université Paris Diderot-Paris 7, Sorbonne Paris Cité, CNRS, UMR 7162,

10, rue A. Domon et L. Duquet, 75205 Paris 13, France

[‡]Research Center in Physics of Matter and Radiation (PMR), Université de Namur, 61 Rue de Bruxelles, 5000 Namur, Belgium

[¶]Institute of Theoretical Physics, Ecole Polytechnique Fédérale de Lausanne (EPFL), CH-1015 Lausanne, Switzerland

[§]New address: Université de Pau et des Pays de l'Adour, IPREM - ECP CNRS UMR 5254, Hélioparc Pau-Pyrénées, 2 av. du Président Angot, 64053 Pau Cedex 9, France

Grain boundaries in epitaxial graphene on the SiC(000 $\bar{1}$) substrate are studied using scanning tunneling microscopy and spectroscopy. All investigated small-angle grain boundaries show pronounced out-of-plane buckling induced by the strain fields of constituent dislocations. The ensemble of observations allows to determine the critical misorientation angle of buckling transition $\theta_c = 19 \pm 2^\circ$. Periodic structures are found among the flat large-angle grain boundaries. In particular, the observed $\theta = 33 \pm 2^\circ$ highly ordered grain boundary is assigned to the previously proposed lowest formation energy structural motif composed of a continuous chain of edge-sharing alternating pentagons and heptagons. This periodic grain boundary defect is predicted to exhibit strong valley filtering of charge carriers thus promising the practical realization of all-electric valleytronic devices.

The unique two-dimensional (2D) structure of graphene endows it with exceptional physical properties and potential applications.^{1,2} Large-area graphene sheets required by technology can be obtained by several scalable production routes such as epitaxial growth on the SiC substrate³ and chemical vapor deposition (CVD) on metal surfaces.⁴ The obtained large-area samples are polycrystalline at micrometer length scales. Grain boundaries (GBs) intrinsically present in polycrystalline graphene significantly affect its properties⁵ including electronic conductivity,^{6,7} thermal conductivity,⁸ mechanical strength⁹ and chemical reactivity.¹⁰ Understanding the structure and properties of GBs in graphene is crucial for the development of graphene-based nanoelectronics.

Importantly, the atomic structure of GB defects depends strongly on the details of the synthetic method used for producing graphene. In CVD graphene, transmission electron microscopy experiments have revealed the disordered aperiodic structure of GBs^{11,12} and recently ordered segments exhibiting van Hove Singularities have been observed.¹³ In contrast, graphene grown on the SiC(000 $\bar{1}$) substrate shows a strong tendency towards forming periodic GBs,^{14,15} akin to those found in highly oriented pyrolytic graphite.^{16–19} Investigating ordered one-dimensional defects in graphene is important as such structures have been proposed as a means of controlling electronic transport in graphene, thus realizing novel devices and extending the capabilities of traditional electronics.^{20,21} Moreover, such structures can be used as a testbed for investigating fundamental

theoretical predictions regarding 2D materials. One such phenomenon is the buckling transition resulting from the interplay between in-plane stress fields, produced by dislocations constituting the GB defects, and the out-of-plane deformation.^{22–24}

In this Letter, we report a comprehensive scanning tunneling microscopy (STM) investigation of GBs in epitaxial graphene on SiC(000 $\bar{1}$) combining atomic resolution imaging and local spectroscopy. A broad statistics of the observed GBs allowed determining the critical misorientation angle for the transition between flat and buckled regimes. A scanning tunneling spectroscopy (STS) investigation of a highly regular large-angle GB reveals the presence of localized electronic states. First-principles calculations allowed this GB to be assigned to the previously predicted lowest formation energy structural motif composed of a continuous chain of edge-sharing alternating pentagons and heptagons. Non-equilibrium Green’s function calculations show that charge carriers transmitted across this periodic defect acquire high valley polarization, thus making it a prospective component of valleytronic devices.

The sample was obtained by annealing a SiC(000 $\bar{1}$) substrate in UHV at 1300°C under a Si flux as previously reported.^{14,25} This method produces multilayer graphene samples with a rotational disorder between adjacent layers. The number of layers was larger than five, as verified by Auger spectroscopy. STM/STS measurements were performed using an Omicron Nanotechnology low temperature STM operating under UHV conditions (less than 10^{-10} mbar) at liquid nitrogen temperature. Local dI/dV spectra were recorded using a lock-in amplifier with a modulation at 711 Hz and 30 mV amplitude. The sample was introduced into the UHV system and outgassed at a temperature of 880° C to remove residual adsorbed molecules. All measurements were performed with electrochemically etched tungsten tips.

Figure 1 shows a representative topographic STM image of epitaxial graphene on SiC(000 $\bar{1}$) covering a 15×15 nm² area. The image reveals three single-crystalline domains with different lattice orientations separated by three GB defects forming a junction in the upper part of the imaged area. Each GB is characterized by a misorientation angle $\theta = \theta_1 - \theta_2$, where θ_1 and θ_2 are the lattice orientations of the two domains with respect to a common reference vector. Below, we adhere

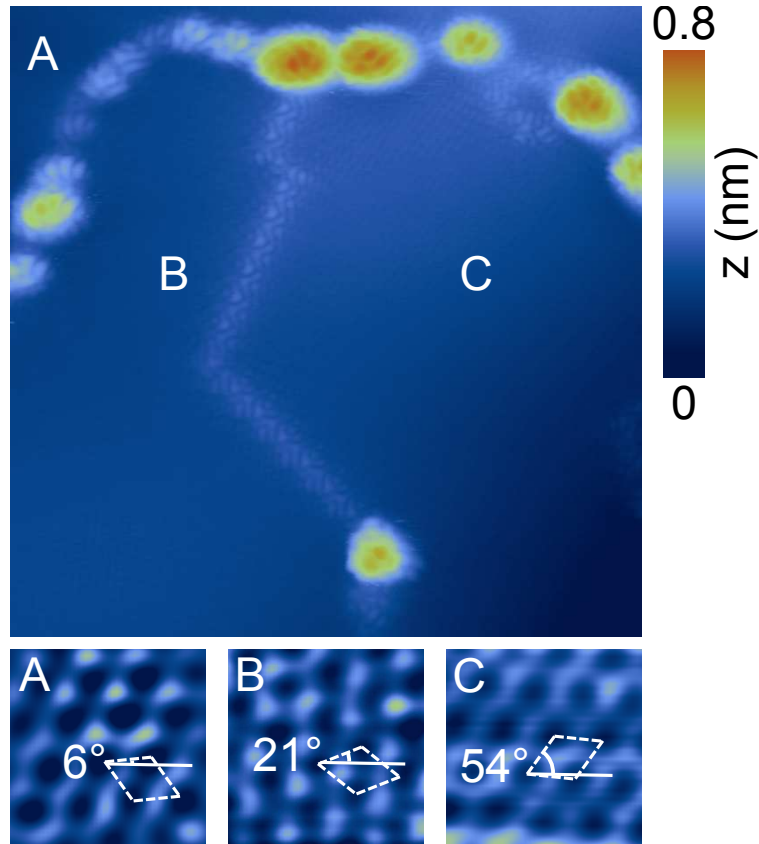


Figure 1: Raw STM image of epitaxial graphene grown on SiC(000 $\bar{1}$) substrate ($15 \times 15 \text{ nm}^2$, $U = 0.75 \text{ V}$, $I = 500 \text{ pA}$) that exhibit three single-crystalline domains with different lattice orientations (labeled A, B and C). The magnified atomic-resolution images ($1 \times 1 \text{ nm}^2$) show the orientation of the three domains with respect to a common reference vector. Buckled (between domains A and B, and domains A and C) and flat (between domains B and C) GBs are observed.

to the convention of Ref.²³ defining misorientation angle in the range $0^\circ < \theta < 60^\circ$ (small-angle grain boundaries thus correspond to θ close to 0° or 60°). We note that the observed GBs show some striking differences in appearance. The GB separating domains B and C is characterized by a misorientation angle $\theta = 33 \pm 2^\circ$ and exhibits a highly ordered structure with clear atomic-scale periodicity. The two linear segments ca. 5 nm long are separated by 120° turn and show identical STM topographies. This periodic structure is characterized by a typical height of 0.07 nm at tunneling bias $U = 0.75$ V. In contrast, the two other GBs separating A and B ($\theta = 16 \pm 3^\circ$) and A and C ($\theta = 48 \pm 4^\circ$) exhibit much larger topographic contrasts with typical heights of 0.26 nm and 0.36 nm, respectively, measured at $U = 0.75$ V. These defects appear as chains of “humps” in which periodicity is respected only approximately. The observed significant topographic contrast is assigned to the out-of-plane deformation. Such buckling in the third dimension represents a physical mechanism unique to 2D systems, which allows relieving the in-plane elastic strain produced by topological defects.^{22,26} The grain-boundary buckling provides a mechanism of relieving the in-plane elastic strain created by individual dislocations that constitute one-dimensional GB defects. The dominant long-range part of this strain field depends on the magnitude of the Burgers vector of dislocations, rather than on the atomic structure of their cores. In large-angle GBs ($\theta \sim 30^\circ$), the distance between neighboring dislocations is comparable to their Burgers vectors, which results in effective mutual cancellation of the strain fields produced by dislocations. Such GBs structures do not undergo buckling. However, for larger and smaller values of GB misorientation angles θ , the distance between neighboring dislocations in GB structures increases,²³ giving rise to buckled structures beyond certain values of critical misorientation angles θ_c .

Corrugation induced by well-separated dislocations have been observed in both epitaxial²⁷ and suspended graphene.²⁸ In the former case, individual dislocations appear in STM image as hump-like features similar to the ones observed in our work.

The total number of investigated GBs is 14, thus allowing us to determine the critical misorientation angle at which transition between flat and buckled regimes takes place. Figure 2 reports the results of our measurements presented as apparent height of GBs as a function of misorientation

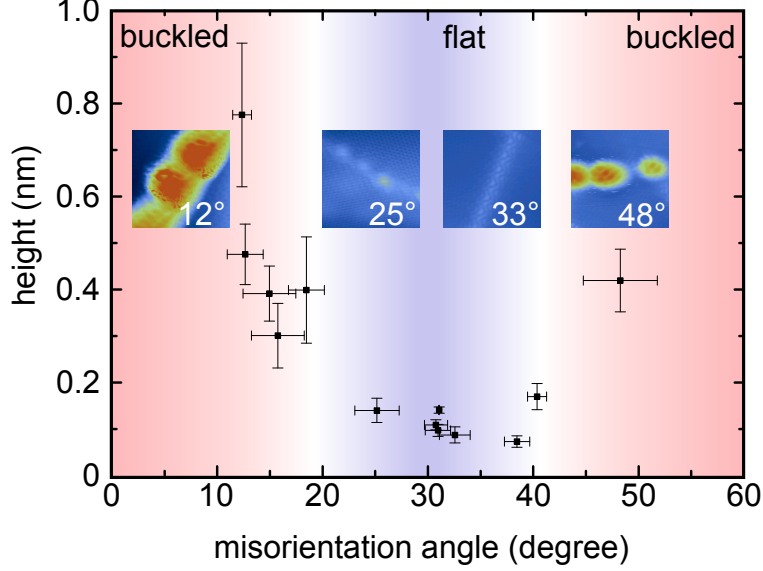


Figure 2: Apparent height of grain boundaries (measured in STM images at $U = 1$ V, $I = 500$ pA) as a function of misorientation angle θ . The insets show representative STM images (5×5 nm²) of buckled and flat GBs corresponding to different misorientation angles θ (same color scale as in Fig. 1).

angle θ . Since STM probes both the surface geometry and electronic effects with the latter being very sensitive to bias voltage, all measurements have been performed at the same bias voltage $U = 1$ V. The uncertainties in measuring the angle are due to piezo drift, and the error bars on the height are due to variations of the apparent height of local maxima. The results in Fig. 2 clearly show that all observed GBs can be divided into two distinct categories defined by an apparent height smaller or larger than 0.2 nm. This feature does not depend critically on the applied bias voltage as (see supporting information Fig. S1). As exemplified in the inset, well-defined periodic structures are observed for the large-angle GBs ($\theta \sim 30^\circ$). Their low apparent height allows assigning these structures to the flat regime. The particular case of $\theta = 25 \pm 2^\circ$ is more ambiguous as its atomic-scale structure is superimposed with a superstructure of 2.6 nm periodicity. In contrast, all small-angle GBs ($\theta \sim 10^\circ$ and $\theta \sim 50^\circ$) display pronounced “humps” of much larger apparent height which allows assigning them to the buckled regime. From the ensemble of data presented we conclude that the transitions between the flat and buckled regimes occur within the ranges $18^\circ < \theta < 25^\circ$ and $40^\circ < \theta < 48^\circ$. We further assume that the critical values of the transition are symmetric with respect to $\theta = 30^\circ$. This assumption is based on the symmetry of graphene

lattice and the fact that the dependence of GB energies on θ is roughly symmetric with respect to $\theta = 30^\circ$.²³ By combining the two ranges of buckling transition we estimated the value of the critical angle $\theta_c = 19 \pm 2^\circ$, with corresponding symmetric transition taking place at $\theta_c = 41 \pm 2^\circ$. The obtained value fully agrees with the results of first-principles calculations in which only the periodic GB models characterized by $\theta = 21.8^\circ$, 32.2° and 38.2° belong to the flat phase.²³

We now focus our attention on the electronic properties of the highly ordered flat GB with $\theta = 33 \pm 2^\circ$ discussed above. Figure 3(a–d) shows the topographic images obtained at different bias voltages ($U = -1$ V, 0.35 V, 0.45 V and 0.75 V). At three positive bias voltages we observe the same periodic pattern, while a different motif is seen at negative bias. The bias dependence of the image suggests significant differences of the electronic structure at positive and negative biases. Figure 3(e) compares dI/dV spectra measured above the grain boundary (red curve) and inside a single-crystalline domain of graphene far from the GB (black curve). Inside the graphene domain the dI/dV spectrum has a typical V-shaped curve with a minimum close to the Fermi level corresponding to the Dirac point. In contrast, sharp and intense peaks are observed in the dI/dV spectrum of the GB at 0.38 V, 0.48 V and 0.75 V. Interestingly, these peaks vanish at the 120° junction of the GB [center left of Fig. 1] as shown by the green curve in Fig. 3(e). Similarly, no dI/dV peak was observed in the case of buckled GB between domains A and B of Fig. 1 [blue curve in Fig. 3(e)]. The three peaks measured in the dI/dV spectrum are therefore characteristic of the $\theta = 33 \pm 2^\circ$ GB. The spatial distribution of the electronic states was probed by mapping the dI/dV signal that corresponds to the local density of states (LDOS). The inset of Fig. 3(e) shows such a conductance map recorded at 0.75 V and projected on the topography image of the GBs. The conductance map clearly shows that the peak at 0.75 V corresponds to an electronic state localized on the linear segments of the GB. Detailed information on the atomic scale variation of the experimental spectroscopy and dI/dV maps are given in the supporting information Fig. S2.

The measured misorientation angle $\theta = 33 \pm 2^\circ$ provides a strong suggestion of the possible structure of this GB. Indeed, a symmetric GB structure with $\theta = 32.2^\circ$ ($\theta_1 = -\theta_2 = 16.1^\circ$) proposed in Ref.²³ represents a continuous chain of edge-sharing pentagons and heptagons [Fig. 4(a)].

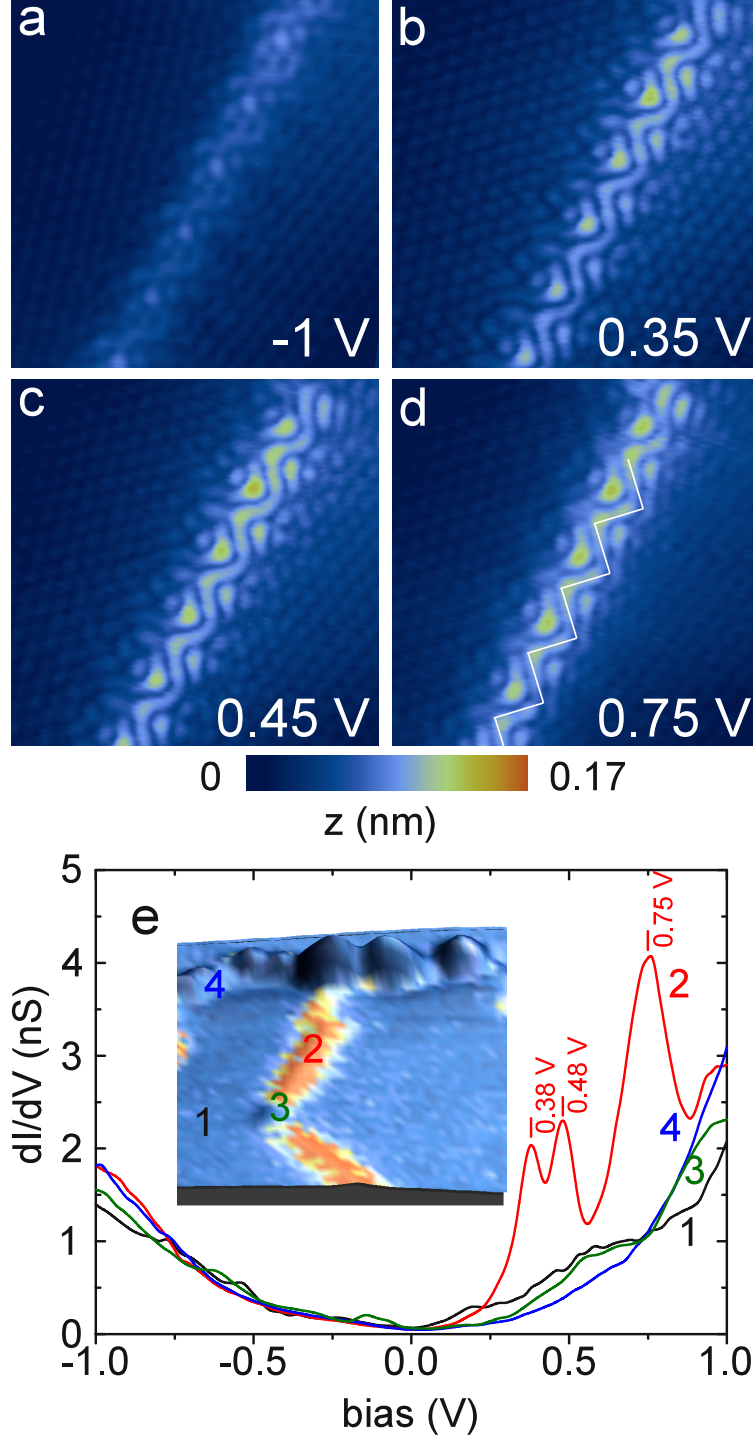


Figure 3: (a–d) Topographic STM images ($4.5 \times 4.5 \text{ nm}^2$) of the $\theta = 33 \pm 2^\circ$ grain boundary shown in Fig. 1 measured at different bias voltages U and the tunneling current $I = 500 \text{ pA}$. The white broken line in (d) is a guide to the eye indicating the zigzag pattern of the central part of the grain boundary. (e) dI/dV spectra measured on the graphene sheet (black), on the grain boundary (red), at the kink of the grain boundary (green) and on the buckled grain boundary between domains A and C areas in Fig. 1 (blue). Inset: Composite 3D topographic image ($5 \times 5 \text{ nm}^2$) color coded with the conductance map at 0.75 V (blue: low conductance, red: high conductance) showing the area where the dI/dV spectra were measured.

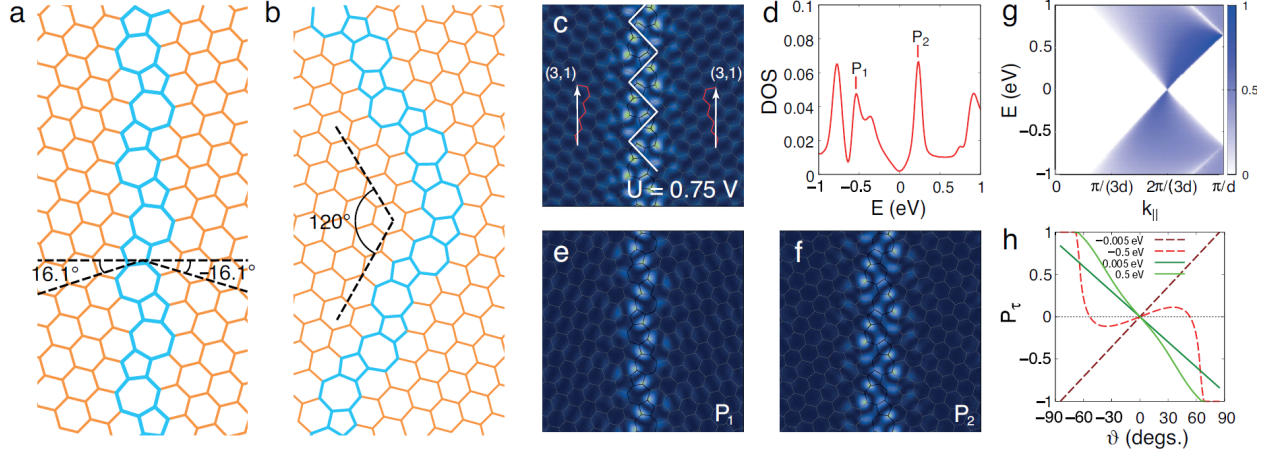


Figure 4: Atomistic models of (a) the $\theta = 32.2^\circ$ symmetric GB ($\theta_1 = -\theta_2 = 16.1^\circ$) and (b) its 120° junction. Pentagons and heptagons are highlighted. (c) Simulated STM image of the $\theta = 32.2^\circ$ GB ($5 \times 5 \text{ nm}^2$, bias voltage $U = 0.75 \text{ V}$). The white broken line is a guide to the eye (same scale as in Fig. 3(d)) indicating the zigzag pattern of the central part of the grain boundary. Its periodicity is further indicated by matching vectors²⁰ $(3,1) = 0.9 \text{ nm}$. (d) Density of states plot of the $\theta = 32.2^\circ$ GB calculated from first principles. (e,f) Simulated dI/dV maps at energies corresponding to the DOS peaks labeled P_1 and P_2 in panel (d). (g) Charge-carrier transmission probability $T(k_{\parallel}, E)$ across the $\theta = 32.2^\circ$ GB as a function of momentum along the GB k_{\parallel} and energy E calculated using the tight-binding model. Half of the Brillouin zone ($0 < k_{\parallel} < \pi/d$, where $d = 0.89 \text{ nm}$ is the periodicity of $\theta = 32.2^\circ$ GB) and one valley are shown for clarity. (h) Valley polarization $P_{\tau}(\vartheta, E)$ of charge-carriers transmitted through the GB defect as a function of incidence angle ϑ at different energies.

Such a structure has been recently observed by STM on graphene on SiO₂.¹³ The dI/dV spectra reported on SiO₂ differ from the spectra we measured on SiC. We attribute this to the difference of sample roughness and structure in proximity to the GB and possibly the difference of supporting substrate. All carbon atoms in this structure maintain their original threefold coordination. Importantly, the observed 120° turn can be introduced with minimal changes to the arrangement of pentagons and heptagons [Fig. 4(b)]. In order to verify this hypothesis we perform first-principles simulations²⁹ of the STM images within the Tersoff-Hamann approximation.³⁰ The simulated STM image, assuming bias voltage $U = 0.75$ V, is shown in Fig. 4(c). The qualitative features appear to be identical to those of the experimental STM images recorded at positive bias voltages [Fig. 3(b–d)]. In particular, experimental images reveal a periodic zigzag pattern with bright spots in the corners. The simulated STM images show extra nodal lines crossing the zigzag, which are likely not resolved in the experimental images. However, we note the periodicity of the zigzag patterns (0.9 nm) in actual and simulated STM images coincides, as indicated by the broken lines displayed in Fig. 3(d) and Fig. 4(c) that have the same scale. This STM signature is due to the localized electronic states with large weights on the carbon atoms belonging to pentagons and heptagons. The properties of these localized electronic states are further elaborated with the help of the density-of-states (DOS) plot shown in Fig. 4(d). In particular, we observe a pair of van Hove singularities at positive and negative energies [labeled P₁ at $E = -0.55$ eV and P₂ at $E = 0.25$ eV in Fig. 4(d)], which is characteristic to GBs in graphene.³¹ We note, however, that the position of the peaks do not agree with the dI/dV spectrum shown in Fig. 3(e). This disagreement is likely to be a consequence of compressed energy scales typical to ordinary density-functional-theory calculations as well as due to tip-induced effects.³² The combination of these two factors shifts both peaks observed in STS measurements to higher absolute energies compared to our first-principles calculations. The experimental counterpart of the negative-energy peak P₁ is likely to be out of scale in the measurements. The simulated dI/dV maps in Fig. 4(e,f) nevertheless show qualitative agreement with corresponding experimental images [Fig. 3(a–d) and supporting information Fig. S2].

Misorientation angle is defined by the orientation of graphene seeds, which is related mostly to the kinetic aspects of the initial stages of the growth process. On the contrary, the atomic structure of GBs can be strongly influenced by local equilibrium aspects. The observation of highly ordered GBs implies that the growth process of our epitaxial graphene on SiC(000 $\bar{1}$) allows approaching local thermodynamic equilibrium closer than, for instance, CVD growth on the Cu surface,⁴ which typically results in more disordered large-angle GBs.^{11,12} Indeed, the morphology of the polycrystalline graphene and the structure of GBs present in it depend strongly on the growth method used to synthesize graphene.³³ Moreover, the observation of the $\theta = 32.2^\circ$ symmetric GB is not surprising considering the fact that this structural motif, first predicted in Ref.,²³ corresponds to the minimum of the GB energy vs. misorientation angle curve ($E_f = 0.284 \text{ eV/\AA}$).

Ordered line defects in graphene have been predicted to exhibit novel transport phenomena originating from the conservation of momentum $k_{||}$ along the defect.^{20,21} Below, we reveal the transport properties of the $\theta = 32.2^\circ$ GB by means of a theoretical investigation. Periodicity of the discussed $\theta = 32.2^\circ$ GB is defined by matching vector indices $(n_L, m_L) = (n_R, m_R) = (3, 1)$, which identifies this line defect structure as class Ib GB, according to the classification introduced in Ref.²⁰ No transport gap is expected in this case, but the two valleys $\tau = +1$ and $\tau = -1$ are separated in $k_{||}$ suggesting that this GB structure can exhibit valley polarized transport properties similar to the 5–5–8 line defect discussed previously.^{21,34} Figure 4(g) shows the ballistic charge-carrier transmission probability $T(k_{||}, E)$ across this GB as a function of momentum $k_{||}$ and energy E calculated using the non-equilibrium Green's function approach and the nearest-neighbor tight-binding Hamiltonian $H = -t \sum_{\langle i, j \rangle} [c_i^\dagger c_j + \text{h.c.}]$ ($t = 2.7 \text{ eV}$).² The magnitude of the transmission probability $T(k_{||}, E)$ shows significant variations upon changing $k_{||}$, and hence the incidence angle ϑ of ballistic charge carriers. This effect is particularly pronounced for electrons ($E > 0$) where $T(k_{||}, E)$ increases monotonically with increasing $k_{||}$ at constant E . The opposite tendency is observed for the hole charge carriers ($E < 0$) with the dependence practically vanishing at $E \approx -0.5 \text{ eV}$. The calculated valley polarization of ballistic charge carriers expressed as a

function of their incidence angle ϑ

$$P_{\tau}(\vartheta, E) = \frac{T_{\tau=+1}(\vartheta, E) - T_{\tau=-1}(\vartheta, E)}{T_{\tau=+1}(\vartheta, E) + T_{\tau=-1}(\vartheta, E)}$$

for several different values of energy E is shown in Fig. 4(h). Apart from the case of high-energy hole charge carriers ($E = -0.5$ eV), P_{τ} exhibits an almost linear dependence on ϑ with complete valley polarization achievable at oblique incidence angles. Such a simple dependence is largely due to the absence of strong resonant backscattering characteristic to the 5–5–8 line defect.³⁵

In conclusion, our combined STM and theory study reveals that grain-boundary defects in epitaxial graphene on the SiC(000 $\bar{1}$) substrate tend to form highly ordered structures. This opens novel opportunities for tailoring electronic and transport properties of graphene, in particular, for realizing valleytronic devices^{36,37} in which valley polarization is controlled by all-electric means. In addition, the observation of a sufficiently large number of flat and corrugated grain boundaries allowed determining the critical misorientation angle of buckling transition $\theta_c = 19 \pm 2^\circ$, thus confirming previous theoretical predictions.

Acknowledgement

V.R. thanks the Institut Universitaire de France for support. Y. T. thanks the Labex SEAM program No. ANR-11-LABX-086 for financial support in the framework of the Program No. ANR-11-IDEX-0005-02. F.G. and O.V.Y. acknowledge financial support of the Swiss National Science Foundation (grant No. PP002P_133552). First-principles calculations have been performed at the Swiss National Supercomputing Centre (CSCS) under projects s443 and s515.

Supporting Information Available

Additional experimental data for bias dependent imaging of the GBs and dI/dV maps of the $\theta = 33 \pm 2^\circ$ GB. This material is available free of charge via the Internet at <http://pubs.acs.org/>.

References

- (1) Novoselov, K. S.; Geim, A. K.; Morozov, S. V.; Jiang, D.; Zhang, Y.; Dubonos, S. V.; Grigorieva, I. V.; Firsov, A. A. *Science* **2004**, *306*, 666–669.
- (2) Neto, A. H. C.; Guinea, F.; Peres, N. M. R.; Novoselov, K. S.; Geim, A. K. *Rev. Mod. Phys.* **2009**, *81*, 109–162.
- (3) Berger, C.; Song, Z.; Li, X.; Wu, X.; Brown, N.; Naud, C.; Mayou, D.; Li, T.; Hass, J.; Marchenkov, A. N.; Conrad, E. H.; First, P. N.; de Heer, W. A. *Science* **2006**, *312*, 1191–1196.
- (4) Li, X.; Cai, W.; An, J.; Kim, S.; Nah, J.; Yang, D.; Piner, R.; Velamakanni, A.; Jung, I.; Tutuc, E.; Banerjee, S. K.; Colombo, L.; Ruoff, R. S. *Science* **2009**, *324*, 1312–1314.
- (5) For review see Yazyev, O. V.; Chen, Y. P. *Nature Nanotechnol.*, in press.
- (6) Yu, Q.; Jauregui, L. A.; Wu, W.; Colby, R.; Tian, J.; Su, Z.; Cao, H.; Liu, Z.; Pandey, D.; Wei, D.; Chung, T. F.; Peng, P.; Guisinger, N. P.; Stach, E. A.; Bao, J.; Pei, S.-S.; Chen, Y. P. *Nature Mater.* **2011**, *10*, 443–449.
- (7) Tsen, A. W.; Brown, L.; Levendorf, M. P.; Ghahari, F.; Huang, P. Y.; Havener, R. W.; Ruiz-Vargas, C. S.; Muller, D. A.; Kim, P.; Park, J. *Science* **2012**, *336*, 1143–1146.
- (8) Vlassioun, I.; Smirnov, S.; Ivanov, I.; Fulvio, P. F.; Dai, S.; Meyer, H.; Chi, M.; Hensley, D.; Datskos, P.; Lavrik, N. V. *Nanotechnology* **2011**, *22*, 275716.
- (9) Grantab, R.; Shenoy, V. B.; Ruoff, R. S. *Science* **2010**, *330*, 946–948.
- (10) Malola, S.; Häkkinen, H.; Koskinen, P. *Phys. Rev. B* **2010**, *81*, 165447.
- (11) Huang, P. Y.; Ruiz-Vargas, C. S.; van der Zande, A. M.; Whitney, W. S.; Levendorf, M. P.; Kevek, J. W.; Garg, S.; Alden, J. S.; Hustedt, C. J.; Zhu, Y.; Park, J.; McEuen, P. L.; Muller, D. A. *Nature* **2011**, *469*, 389–392.

- (12) Kim, K.; Lee, Z.; Regan, W.; Kisielowski, C.; Crommie, M. F.; Zettl, A. *ACS Nano* **2011**, *5*, 2142–2146.
- (13) Ma, C.; Sun, H.; Zhao, Y.; Li, B.; Li, Q.; Zhao, A.; Wang, X.; Luo, Y.; Yang, J.; Wang, B.; Hou, G., *J. Phys. Rev. Lett.* **2014**, *112*, 226802.
- (14) Varchon, F.; Mallet, P.; Magaud, L.; Veuillen, J.-Y. *Phys. Rev. B* **2008**, *77*, 165415.
- (15) Biedermann, L. B.; Bolen, M. L.; Capano, M. A.; Zemlyanov, D.; Reifenberger, R. G. *Phys. Rev. B* **2009**, *79*, 125411.
- (16) Marchon, B.; Ferrer, S.; Kaufman, D. S.; Salmeron, M.; Siekhaus, W. *Thin Solid Films* **1987**, *154*, 65–73.
- (17) Albrecht, T. R.; Mizes, H. A.; Nogami, J.; Park, S.-i.; Quate, C. F. *Appl. Phys. Lett.* **1988**, *52*, 362–364.
- (18) Simonis, P.; Goffaux, C.; Thiry, P. A.; Biro, L. P.; Lambin, P.; Meunier, V. *Surf. Sci.* **2002**, *511*, 319–322.
- (19) Červenka, J.; Flipse, C. F. J. *Phys. Rev. B* **2009**, *79*, 195429.
- (20) Yazyev, O. V.; Louie, S. G. *Nature Mater.* **2010**, *9*, 806–809.
- (21) Gunlycke, D.; White, C. T. *Phys. Rev. Lett.* **2011**, *106*, 136806.
- (22) Carraro, C.; Nelson, D. R. *Phys. Rev. E* **1993**, *48*, 3082–3090.
- (23) Yazyev, O. V.; Louie, S. G. *Phys. Rev. B* **2010**, *81*, 195420.
- (24) Liu, Y.; Yakobson, B. I. *Nano Lett.* **2010**, *10*, 2178–2183.
- (25) Van Bommel, A.; Crombeen, J.; Van Tooren, A. *Surf. Sci.* **1975**, *48*, 463–472.
- (26) Seung, H. S.; Nelson, D. R. *Phys. Rev. A* **1988**, *38*, 1005–1018.

- (27) Coraux, J.; N'Diaye, A. T.; Busse, C.; Michely, T. *Nano Lett.* **2008**, *8*, 565–570.
- (28) Lehtinen, O.; Kurasch, S.; Krashennnikov, A. V.; Kaiser, U. *Nature Commun.* **2013**, *4*, 2098.
- (29) Soler, J. M.; Artacho, E.; Gale, J. D.; Garcia, A.; Junquera, J.; Ordejon, P.; Sanchez-Portal, D. *J. Phys.: Condens. Matter* **2002**, *14*, 2745–2779.
- (30) Tersoff, J.; Hamann, D. R. *Phys. Rev. B* **1985**, *31*, 805–813.
- (31) Gargiulo, F.; Yazyev, O. V. *Nano Lett.* **2013**, *14*, 250–254.
- (32) McEllistrem, M.; Haase, G.; Chen, D.; Hamers, R. J. *Phys. Rev. Lett.* **1993**, *70*, 2471–2474.
- (33) Biró, L. P.; Lambin, P. *New J. Phys.* **2013**, *15*, 035024.
- (34) Lahiri, J.; Lin, Y.; Bozkurt, P.; Oleynik, I. I.; Batzill, M. *Nature Nanotechnol.* **2010**, *5*, 326–329.
- (35) Chen, J. H.; Autès, G.; Alem, N.; Gargiulo, F.; Gautam, A.; Linck, M.; Kisielowski, C.; Yazyev, O. V.; Louie, S. G.; Zettl, A. *Phys. Rev. B* **2014**, *89*, 121407.
- (36) Rycerz, A.; Tworzydło, J.; Beenakker, C. W. J. *Nature Phys.* **2007**, *3*, 172–175.
- (37) Xiao, D.; Yao, W.; Niu, Q. *Phys. Rev. Lett.* **2007**, *99*, 236809.

Graphical TOC Entry

